



1 **Estimation of Nighttime Aerosol Optical Depths Using** 2 **the Ground-based Microwave Radiometer**

3 Guanyu Liu¹, Jing Li^{1*}, Sheng Yue¹, Lulu Zhang¹, Chongzhao Zhang¹

4 ¹ Department of Atmospheric and Oceanic Sciences, School of Physics, Peking
5 University, Beijing, China

6 Corresponding authors: Jing Li (jing-li@pku.edu.cn)

7 **Abstract**

8 Aerosol optical depth (AOD) is a crucial parameter for understanding the impact of
9 aerosols on Earth's atmosphere and air quality. However, existing remote sensing
10 methods mostly rely on the shortwave spectrum, which does not allow measurements
11 at nighttime. In this study, we made a first attempt to retrieve AOD from
12 ground-based microwave radiometer (MWR) measurements. Brightness temperatures
13 (BT) at the K band (from 22.23 GHz to 30.00 GHz) and V band (from 51.25 GHz to
14 58.80 GHz) are trained against daytime spectral AOD from sun-photometer
15 measurements together with temperature profile using the random forest regression
16 (RFR) retrieval model, and the model is then used to retrieve nighttime AOD. The
17 algorithm demonstrates satisfactory performance, with strong agreements with lunar
18 AOD retrievals. The results also reveal a distinct day-night cycle of AOD, with
19 nighttime AOD typically higher than its daytime value. The physical basis of our
20 approach is verified using vertical temperature and humidity profiles from sounding
21 observation and simulation results from WRF-Chem as well as the MonoRTM. Our
22 study provides an effective and convenient approach to estimate nighttime aerosol
23 loading from surface, which has great potential in environmental monitoring and
24 climate forcing research.

25



26 **1. Introduction**

27 Aerosols have a significant impact on weather patterns and the Earth's climate (Huang
28 et al., 2014; Li et al., 2022; Li et al., 2019; Riemer et al., 2019), offsetting about
29 one-third of the warming effect by anthropogenic greenhouse gases and influence
30 large-scale circulation (Huang et al., 2014; Li et al., 2022). However, accurately
31 assessing their role in radiative forcing is a major challenge (Fan et al., 2016; Ghan et
32 al., 2016; Seinfeld et al., 2016). Monitoring aerosol optical depth (AOD) is crucial for
33 understanding aerosol impacts on climate and air quality, as it reflects the total
34 amount of aerosols in the atmosphere optically (Visioni et al., 2023; Yang et al.,
35 2020). As a result, there have been extensive efforts to measure AOD by various
36 methods.

37 Remote sensing, either ground based or space borne, is an effective way to retrieve
38 column AOD (Chaikovsky et al., 2020; Mhawish et al., 2017; Omar et al., 2013;
39 Sinyuk et al., 2020). Other observations measure physicochemical properties of
40 aerosols instead of optical properties like AOD (Kremser et al., 2016; Li et al., 2016b).
41 Mainstream aerosol remote sensing techniques rely on aerosol scattering of shortwave
42 radiation in the ultraviolet and/or visible spectrum, thus only daytime AOD can be
43 obtained (Sayer et al., 2019; Sun et al., 2021). However, aerosols typically have
44 day-night variability, due to factors such as different emission sources, boundary layer
45 structure, etc (Arola et al., 2013; Cachorro et al., 2004; Cachorro et al., 2008; Guo et
46 al., 2017). Aerosols at nighttime also have detectable impacts on the radiative balance,
47 since they usually exert a warming effect in contrast to the cooling effect at daytime
48 (Chen and Zhao, 2024; Colarco et al., 2014; Zhang et al., 2022), particularly in polar
49 regions with the rapid change of AOD between daytime and nighttime (Chen and
50 Zhao, 2024; Stenchikov et al., 2002; Wei et al., 2021). In special cases such as
51 aerosols above the open oceans, they consistently exert a cooling influence in both
52 shortwave and longwave, yet for dust aerosols, they potentially exert a warming effect



53 in longwave during both day and night (Adebiyi et al., 2023; Feng et al., 2022; Song
54 et al., 2022).

55 Remote sensing of aerosol properties at night is a challenging task. Lunar photometer
56 emerges during recent years as an effective and relative accurate nighttime AOD
57 retrieval technique, and has been widely used within the Aerosol Robotic Network
58 (AERONET) (Barreto et al., 2016). However, this method can only provide data at ~
59 halftime each month since it requires a relatively large amount of moon-reflected
60 solar radiation (Barreto et al., 2017; Berkoff et al., 2011). Compared with lunar
61 photometer method, the star photometry provides reliable nighttime AOD
62 measurements by leveraging stellar irradiance, eliminating lunar phase corrections,
63 with long-term datasets revealing diurnal aerosol dynamics (Pérez-Ramírez et al.,
64 2011; Pérez-Ramírez et al., 2016; Pérez-Ramírez et al., 2008; Pérez-Ramírez et al.,
65 2015). Arctic deployments and further development such as using a wide-field imager
66 enhance its adaptability in extreme environments and spatiotemporal resolution,
67 addressing gaps in traditional sun-photometer-based nocturnal monitoring (Ebr et al.,
68 2021; Ivanescu et al., 2021; Ivanescu and O'Neill, 2023). Other researches take
69 advantage of urban light to retrieve nighttime AOD from space from multiple sensors
70 (Jiang et al., 2022; Meng et al., 2023; Wang et al., 2023; Wang et al., 2020; Zhou et
71 al., 2021). For example, Zhang et al. examined the effectiveness of retrieving
72 nighttime AOD over urban areas by utilizing city lights observed through the VIIRS
73 (Visible Infrared Imaging Radiometer Suite) Day-Night Band (DNB) (Zhang et al.,
74 2019). However, this approach has limitations as it does not account for multiple
75 scattering and gas absorption, which can potentially reduce the signals from aerosols
76 (Zhou et al., 2021). Furthermore, these studies are constrained to the spatial scale of
77 urban areas, resulting in vast rural regions being unexplored (Meng et al., 2023).
78 Active remote sensing, such as lidars, can provide aerosol measurements at both day
79 and night time (Balmes et al., 2021; Jiang et al., 2024). Nonetheless, solving the lidar
80 equation requires assumption of the lidar ratio, and this assumed lidar ratio often



81 causes large uncertainty of the retrieved extinction profiles as well as column
82 integrated AOD usually (Liu et al., 2018; Rogers et al., 2014; Santa Maria and Winker,
83 2005). For the day-night difference of AOD, previous studies find slight increases of
84 nighttime AOD using the long-term sun-and-star photometry data (Pérez-Ramírez et
85 al., 2012; Pérez-Ramírez et al., 2016; Wang et al., 2004). Moreover, using Infrared
86 Atmospheric Sounder Interferometer (IASI) and Cloud-Aerosol Transport System
87 (CATS) are also effective methods to understand day-night differences in dust
88 aerosols (Tindan et al., 2023; Yu et al., 2021). However, existing research regarding
89 day-night difference of AOD only focuses on special types of aerosols such as dust
90 aerosols, and has low availability due to the moon phase and urban light extent
91 (Barreto et al., 2017; Jiang et al., 2022; Meng et al., 2023; Wang et al., 2023; Wang et
92 al., 2020; Zhou et al., 2021). Due to our limited capability to measure nighttime AOD,
93 there is a significant knowledge gap between daytime and nighttime aerosol
94 properties.

95 In contrast to shortwave radiation which is only available during daytime, longwave
96 radiation, especially in the thermal infrared and microwave spectrum, exists during
97 both day and night, and offers the potential to derive nighttime aerosol property
98 (Dufresne et al., 2002; Panicker et al., 2008). Previous research has explored the
99 possibility to retrieve aerosol loading using longwave measurements, but mostly
100 focused on large particles such as dust (Clarisse et al., 2019; Desouza-Machado et al.,
101 2010; Klüser et al., 2012; Pierangelo et al., 2004; Pierangelo et al., 2005; Zheng et al.,
102 2022; Zheng et al., 2023). For example, using collocated thermal infrared
103 observations from MODIS and dust optical depth from Cloud-Aerosol Lidar with
104 Orthogonal Polarization (CALIOP), Zheng et al. simultaneously retrieve the thermal
105 infrared dust optical depth and coarse-mode effective diameter over global oceans
106 (Zheng et al., 2023). Observational and simulation studies indicate that the microwave
107 brightness temperatures (BTs) and brightness temperature polarization differences
108 may be both useful for estimating the dust mass loading (Ge et al., 2008; Hong et al.,



109 2008; Huang et al., 2007; Mitra et al., 2013). Our previous study utilized
110 satellite-based thermal infrared measurements in the atmospheric window region to
111 retrieve nighttime AOD (Liu et al., 2024), and proves the effectiveness of these
112 longwave measurements in deriving aerosol properties.

113 Ground-based microwave radiometer (MWR) is a widely used remote sensing
114 instrument to retrieve temperature and humidity profiles using emitted longwave
115 radiation by the surface-atmosphere system (Bianco et al., 2005; Greenwald et al.,
116 2018; Knupp et al., 2009). Considering the aforementioned concepts of utilizing
117 longwave radiances to retrieve aerosol properties and the potential alterations in
118 microwave BTs due to the modified temperature and humidity profiles resulting from
119 the shortwave radiation effect of aerosols, there is potential that aerosol information
120 can be derived from MWR measurements. Therefore, in this study, we explore the
121 possibility to retrieve AOD using surface based MWR measurements in the K spectral
122 bands (22.23 GHz, 22.50 GHz, 23.03 GHz, 23.83 GHz, 25.00 GHz, 26.23 GHz, 28.00
123 GHz, and 30.00 GHz) and V spectral bands (51.25 GHz, 51.76 GHz, 52.28 GHz,
124 52.80 GHz, 53.34 GHz, 53.85 GHz, 54.40 GHz, 54.94 GHz, 55.50 GHz, 56.02 GHz,
125 56.66 GHz, 57.29 GHz, 57.96 GHz, and 58.80 GHz). A machine learning based
126 algorithm is developed to estimate AOD during both day and night. The theoretical
127 basis of the method is further verified using regional model and radiative transfer
128 simulations. The difference between day and night time AOD is also examined using
129 the retrieval results.

130 **2. Data and Methods**

131 The retrieval algorithm used in this study is described in Figure 1 and includes four
132 main steps: (1) preprocessing of input variables, (2) training the Random Forest
133 Regression (RFR) retrieval model, (3) estimation of AOD using the trained model,
134 and (4) independent validation to refine the model and assess its performance



135 compared to lunar photometer observations. The details of the datasets and methods
136 are explained below.

137 **2.1 Datasets**

138 In this study, we utilized BT data collected from the MP-3000A MWR, which was
139 stationed at the Beijing Nanjiao Meteorological Observatory located in China
140 (39.80°N, 116.47°E). The MP-3000A MWR is capable of detecting signals in the
141 K-band (22 to 30 GHz) and V-band (51 to 59 GHz), and it is also equipped with
142 additional features such as a precipitation sensor, an infrared radiation thermometer,
143 and other relevant instruments. To maintain the accuracy and consistency of the
144 atmospheric BT measurements, the MWR undergoes regular real-time calibration.
145 These measurements are essential for obtaining temperature profiles and AOD data.
146 Our analysis focuses on the K and V band of BT observations with 22 available
147 channels, because BT observations at the K band are sensitive to water vapor
148 absorption and BT observations at the V band are sensitive to oxygen absorption and
149 temperature changes. We use the data ranging from December 2019 to October 2020
150 with a temporal resolution of one minute.

151 The measured BTs include inaccuracies and unusual values caused by instrumental
152 faults, calibration problems, and environmental factors. Hence, it's crucial to conduct
153 quality control (QC) checks on the BT data before processing it further. These checks
154 involve removing abnormal values to ensure that the BTs fall within a reasonable
155 temperature range of 2.7 to 330 Kelvin, and inspecting for data consistency over time
156 as per the methodology of Zhang et al. (Zhang, 2024). Notably, because the
157 collocation between MWR and Level 2 sun photometer AOD products from the
158 AERONET is already clear-sky data, there is no need to perform cloud screening on
159 the MWR data.



160 AOD retrieved using the solar and lunar methods at the Beijing-CAMS AERONET
161 site, which is the closest site to the MWR location, is used as training and validation
162 data in the retrieval algorithm. For training our model, we utilized Level 2 sun
163 photometer AOD products at the wavelengths of 440nm, 675nm, 870nm, and 1020nm
164 during the day. Version 3 Level 1.5 lunar AOD products at the same wavelengths to
165 validate AOD retrievals at night.

166 Given that MWRs are instrumental in tracking atmospheric temperature and humidity
167 profile changes (Zhang et al., 2024), our method retrieves vertical temperature
168 profiles concurrently. This is achieved by using temperatures at different pressure
169 levels obtained from the European Center for Medium-Range Weather Forecasts
170 (ECMWF) Reanalysis version 5 (ERA-5) as the target for our training. To further
171 assess the accuracy of the model in predicting vertical temperature profiles, we
172 utilized the collocated sounding data obtained from Beijing Meteorological Station
173 (station ID: 54511) during the corresponding time frame. These sounding data were
174 collected twice daily respectively at 0000 and 1200 UTC from December 2019 to
175 October 2020. For the physical interpretation of our retrieval method, we employed
176 collocated vertical profiles of temperature and relative humidity (RH) from the same
177 sounding data under varying aerosol loadings to explore the effects of aerosol loading
178 on the vertical profiles of meteorological variables. These vertical profiles were
179 further utilized to compute BTs using the monochromatic radiative transfer model
180 (MonoRTM).

181 **2.2 Retrieval Algorithm**

182 Because the relationship between aerosol loading and microwave radiation is
183 complicated and could be nonlinear, we use a machine learning based retrieval
184 method focusing on the RFR method (Svetnik et al., 2003). All variables are
185 appropriately matched in both space and time. Specifically, AOD from sun
186 photometer measurements and BTs from the MWR are matched within a 5-minute



187 time window, while hourly temperature profiles from ERA-5 reanalysis datasets and
188 BTs from the MWR are collocated within a 30-minute time window and a 15 km
189 spatial radius.

190 We first apply the relative importance feature selection technique, which is based on
191 the Gini importance measure (Nembrini et al., 2018), to identify significant
192 independent variables and build a generalized model. The relative importance of each
193 factor is presented in Figure 2. It is observed that BTs across various frequency bands
194 carry similar levels of importance, suggesting that the BTs are almost equally
195 important for retrieving AOD.

196 Subsequently, the retrieval algorithm is trained using eight selected K-band BTs as
197 input and target variables, which include sun photometer AOD at 440nm, 675nm,
198 870nm, and 1020nm, as well as ERA-5 vertical temperature profiles at 100 hPa, 200
199 hPa, 500 hPa, 700 hPa, 850 hPa, and 1000 hPa. To ensure the representativeness of
200 the sampling, we select the first 3/4 of the data in each month as the training set and
201 the last 1/4 of the data as the testing set. Additionally, the algorithm is adapted to
202 estimate nighttime AOD using nighttime BTs from microwave radiometry as inputs,
203 which is then validated against nighttime AOD observations from lunar measurements
204 in lunar photometer for the same period. Moreover, AOD, whether in the visible or
205 microwave region, is associated with aerosol loading, which serves as the foundation
206 for retrieving visible AOD using microwave observations. Since we primarily aim at
207 retrieving AOD rather than aerosol type, we did not consider AOD at the other
208 wavelengths when building the AOD retrieval model. The relationship between AOD
209 at 550nm and that at the microwave band is enclosed in the random forest model. The
210 model performance is assessed against photometer retrievals using metrics such as
211 linear regression slope and intercept, correlation coefficient (R), root-mean-square
212 error (RMSE), and mean absolute percentage error (MAPE).



213 The RFR model is built by varying the number of decision trees from 8 to 256.
214 Through validation analysis, it is determined that the optimal number of trees is 128,
215 based on the best performance during validation. After refining the algorithm through
216 extensive training and testing, it is used to retrieve nighttime AOD from nighttime
217 MWR BTs, with validation against collocated lunar AOD measurements from the
218 lunar photometer. Moreover, before investigating the diurnal cycle of MWR derived
219 AOD, we perform a quality control on the minute-resolution retrieval results that
220 typically have a higher noise level. Specifically, for each specific minute, we extract
221 the AOD for this minute from each day to form an AOD sequence. We then calculate
222 the mean and standard deviation of this AOD sequence. Finally, we remove AOD that
223 exceeds three times the standard deviation. Considering the suitable quantity of
224 outliers procured by setting the threshold at three standard deviations and the
225 prevalently utilized 3-sigma rule, we used three standard deviations as the threshold
226 (Li et al., 2016a; Liu et al., 2024; Wang et al., 2012).

227 **2.3 WRF-Chem simulations**

228 To investigate the effect of aerosols on downward microwave radiation, we use the
229 Weather Research and Forecasting model with Chemistry (WRF-Chem) simulations
230 combined with the MonoRTM radiative transfer model. Because MWR-observed BT
231 change is not only due to AOD change but also reflects the change of meteorological
232 conditions due to the AOD change, we apply WRF-Chem and MonoRTM radiation
233 transfer model instead of radiative transfer simulations only.

234 WRF-Chem simulation runs from 0000 UTC on 17 December 2016 to 0000 UTC on
235 20 December 2016 (a 72-hour period). The simulation period is different from that of
236 the retrieval because there are no updated emission fields for 2019 and 2020. The
237 initial meteorological conditions used for the simulations are based on the National
238 Center for Atmospheric Research (NCEP) Final Global Forecast System Operational
239 Analysis (FNL) provided by the National Oceanic and Atmospheric Administration



(NOAA), with a $1^{\circ} \times 1^{\circ}$ spatial resolution and a 6-hour temporal interval. The emission fields used here are Emissions Database for Global Atmospheric Research (EDGAR), MIX, and Multi-resolution Emission Inventory for China (MEIC) (Crippa et al., 2018; Li et al., 2017; Wang et al., 2014). The surface emissivity we used for simulation is the default data for WRF-Chem. The simulation domain encompasses the area of Beijing, Tianjin, and Hebei province (as shown in Figure 3), with a center point at 40.00°N , 116.25°E . The model employs a three-tiered nesting configuration, featuring outer grids of 40×46 with a 90 km horizontal spacing, middle grids of 48×60 with a 30 km horizontal spacing, and inner grids of 51×72 with a 10 km horizontal spacing. The vertical atmosphere is segmented into 47 levels, ranging from the model's ground level to 100 hPa, encompassing both the surface and the upper atmosphere. Figure 3 illustrates the domains of the WRF model simulations and the location of the MWR deployed at the Beijing Nanjiao Meteorological Observatory in China. To further confirm our findings, we perform another set of parallel experiments lasting from 0000 UTC on 3 December 2016 to 0000 UTC on 5 December 2016 (a 48-hour period) with the same settings. The first day of both sets of experiments is used for model stabilization, and the subsequent days are utilized for analysis.

For the choices of physical parameterization schemes, we employ the Lin microphysics scheme, the rapid radiative transfer model for global climate model (GCM) applications (RRTMG) for shortwave radiation, the Yonsei University (YSU) boundary layer scheme, the Monin-Obukhov ground layer scheme, the Carbon-Bond Mechanism version Z (CBM-Z) for gas-phase chemistry, and the Model for Simulating Aerosol Interactions and Chemistry (MOSAIC). The model output has a one-hour temporal resolution.

To investigate the responses of surface downward microwave radiation to aerosol loadings, we also conducted two parallel experiments with and without aerosol



emissions in the study. Two simulations that are respectively, designated as “EXP_AER” and “EXP_NOAER” are carried out. The EXP_AER experiment is defined as a control simulation in which aerosol and aerosol precursor emission scheme is turned on. This aerosol emission includes emissions of carbon monoxide, nitrogen oxides, sulphate oxides, dust aerosols, biomass aerosols, biomass burning aerosols, sea salt aerosols and anthropogenic aerosols. The sensitivity experiment (“EXP_NOAER”) is also conducted by closing corresponding aerosol and aerosol precursor emission scheme. The difference between control and sensitivity results are considered as the adjustments of vertical meteorological profiles to aerosol loadings. This method is also widely used to explore the radiative forcing of different kinds of aerosol and its effects on meteorological fields in previous studies (Chen et al., 2023; Matsui et al., 2018).

It is important to note that the aerosol-radiation interaction feature is activated in the WRF-Chem model to investigate the impact of aerosol loadings on meteorological fields. Subsequently, we input meteorological profile data from pollution cases without cloud cover at each grid point into the monochromatic radiative transfer model (MonoRTM) to calculate the corresponding BT responses at various frequencies within the K-band.

2.4 MonoRTM

The MonoRTM, developed by Atmospheric and Environmental Research (AER), is a radiative transfer model specifically designed for microwave and millimeter-wave applications (Clough et al., 2005). This model is particularly useful in the microwave radiation calculation (Payne et al., 2011). In this study, it is used to calculate the brightness temperatures (BTs) associated with the simulated temperature and humidity vertical profiles from WRF-Chem.



292 **3. Results**

293 **3.1 Model fitting and validation**

294 The retrieval model has great fitting performance, as shown by Figure 4. The model
295 fitting reaches correlation coefficients of 0.98 for the 440 nm, 675 nm, 870 nm, and
296 1020 nm, respectively, albeit with a minor systematic low bias for high AOD
297 scenarios, which is similar to MODIS AOD products (Levy et al., 2013). Due to the
298 consistent model performance in all wavelengths (Figure 4), we will focus on results
299 at 440 nm in the following discussions.

300 Figure 5 displays the comparison between the daytime and nighttime AOD
301 independently retrieved by MWR using our algorithm and those from the sun and
302 lunar photometer from December 2019 to October 2020. The model, tested during the
303 daytime, utilized a dataset of over 3,000 samples and achieved correlation coefficients
304 of 0.96 for 440 nm (Figure 5a). Most points are concentrated on the 1:1 line, with
305 RMSE within 0.11 and MAPE within 0.11. The accuracy of this estimation is similar
306 to existing shortwave-based algorithms (Levy et al., 2013). However, the key
307 advantage of using microwave BT is the capability to retrieve AOD at night, a feature
308 lacking in these shortwave-based algorithms (Figure 5b). Nighttime AOD retrieval
309 reaches comparable performance to that for daytime, exhibiting a high correlation of
310 0.91 with lunar AOD. A minor systematic bias towards lower values in high AOD
311 scenarios is also noted, with RMSE about 0.14 and MAPE approximately 0.28,
312 indicating the overall satisfactory performance of MWR retrievals. In addition, the
313 MWR results also well capture the spectral variation of AOD for fine (440 nm to 870
314 nm Angstrom index > 1) and coarse mode particles (440 nm to 870 nm Angstrom
315 index < 1), as shown in Figure 6.

316 Our algorithm simultaneously retrieves daytime and nighttime temperature profiles.
317 As shown in Figure 7 & Figure 8, atmospheric temperature retrieval results also



318 demonstrate good performance and exceed those of AOD. This is expected since the
319 main signals in the microwave come from emitted radiation by the atmosphere that is
320 directly related to temperature. In detail, R is generally above 0.98 and all of the
321 RMSEs are around 1.0 K in the training set (Figure 7). Similarly, for the test set, R is
322 above 0.95 and all of the RMSEs are around 1.8 K the test set (Figure 8), comparable
323 to previous studies using MWR data with an optimal estimation method (Cimini et al.,
324 2006). The significant biases at some pressure levels may be attributed to the larger
325 biases between sounding data and reanalysis data that is used to train the model
326 (Varga and Breuer, 2022). Our model also well captures the characteristics of the
327 climatological mean temperature vertical profile, with the error in each pressure layer
328 within 1.5 K (Figure 9a). There exist greater RMSE and bias in low pressure levels
329 partially due to the higher temperature variations in these levels, the overall RMSE
330 and bias serve to illustrate the exemplary performance of the model in estimating the
331 vertical temperature profiles (Figure 9b & c).

332 In summary, the day and nighttime MWR-based AOD and vertical temperature
333 profiles derived from our algorithm successfully capture the AOD variability and
334 vertical temperature profile characteristics with satisfactory accuracy. This model also
335 unveils the spectral characteristics of AOD, with higher wavelengths corresponding to
336 lower AOD. With great performance through model validation, we will investigate the
337 diurnal cycle of AOD in the following section.

338 **3.2 The diurnal cycle of MWR derived AOD**

339 We further examine the day-night differences in the AOD retrieved by MWR and
340 compare them to those revealed by surface photometer.

341 Figure 10a-b illustrates the mean diurnal cycles of the photometer AOD and
342 MWR-based AOD derived from BT observations at the Beijing Nanjiao
343 Meteorological Observatory in China. As shown in Figure 10a, mean diurnal AOD



344 follows a bi-modal temporal distribution, with a greater peak ~21:00 and a secondary
345 peak at ~03:00. The AOD stays relatively low from 06:00 to 10:00, gradually rises
346 from 10:00 to 21:00, reaching the first peak at 21:00. After that greater peak, the AOD
347 decreases from 22:00 to 00:00, and then increases again until it reaches the second
348 peak at 03:00. This pattern is consistent across other spectral bands (675 nm, 870 nm,
349 and 1020 nm, not shown here). Because the number of nighttime AODs from the
350 photometer is smaller than that during the daytime, but the number of nighttime
351 AODs from the MWR is nearly equal to that during the daytime, this decrease may
352 not be entirely explained by the lack of data sampling and needs further investigation
353 in the future study. Moreover, although the MWR-based AOD seems to underestimate
354 the extreme pollutions with high AOD compared with photometer observation, since
355 the number of upper outliers of AOD of the photometer is higher than that of MWR,
356 the overall temporal pattern is similar to that of the photometer (Figure 10a).

357 The mean and median AOD values further support the above findings, highlighting
358 higher nighttime AOD compared to daytime (Figure 10b). This difference is validated
359 by the boxplots of MWR-based AOD and photometer AOD (Figure 10c), passing the
360 Student's *t*-test significance test with $p \leq 0.05$. Specifically, the median daytime
361 AOD is in the range of 0.15 to 0.28 for MWR and 0.15 to 0.27 for the photometer,
362 while the median nighttime AOD is greater than 0.34 for MWR and higher than 0.30
363 for the photometer. Similarly, the mean daytime AOD is in the range of 0.25 to 0.35
364 for MWR and 0.24 to 0.32 for the photometer, while the mean nighttime AOD is
365 greater than 0.40 for MWR and over 0.44 for the photometer. This discrepancy
366 between daytime and nighttime AOD has also been observed in previous studies
367 estimating nighttime AOD by incorporating infrared radiance measurement from
368 AIRS into the machine learning model (Liu et al., 2024). Notably, the mean AOD
369 tends to exceed the median AOD, partly due to the long-tail distribution of AOD and
370 the presence of high extreme values (Sayer et al., 2019). Moreover, AOD at the other
371 wavelengths (675 nm, 870 nm, and 1020 nm) exhibit similar diurnal patterns with



372 peaks at about 20:00-22:00 (not shown here) and higher nighttime AOD in general
373 (Figure 6).

374 The increase in nighttime AOD compared to daytime can be attributed to various
375 factors, including a shallower mixed layer due to reduced horizontal mixing and
376 transport, a decrease in atmospheric environmental capacity, higher relative humidity,
377 enhanced aerosol hygroscopic growth, or intensified pollution emissions (Brock et al.,
378 2016). Similar observations of elevated nighttime particle matter concentration have
379 been reported in previous studies (Perrone et al., 2022; Su et al., 2023). However,
380 research on nighttime aerosol properties is limited, warranting further analysis to fully
381 understand these discrepancies, which exceeds the scope of this study.

382 In summary, by using the BT measured by the MWR to retrieve AOD during
383 nighttime, we can uncover the daily cycle of AOD. This improves our understanding
384 of the day-nighttime AOD variability, provides insights into the diurnal changes of
385 atmospheric pollution and sheds light on nighttime aerosol radiative effects.

386 **3.3 Physical interpretation**

387 Since the machine learning technique does not necessarily represent the physical
388 relationship between aerosol loading and microwave radiances, we further verify the
389 theoretical basis of our technique by analyzing the observed temperature and RH
390 profiles under various AOD levels and using WRF-Chem combined with MonoRTM
391 simulations. A set of sensitivity experiments with and without aerosol forcing is
392 conducted using WRF-Chem as described in Section 2, whose atmospheric profiles,
393 including temperature, water vapor, gases and aerosols, are then used as the inputs to
394 the MonoRTM to simulate the downward microwave radiances (represented by BT)
395 observed by the MWR. To mitigate the influence of surface temperature on BT, we
396 maintained a consistent surface temperature range (265 K-270 K) throughout the
397 simulation.



398 We first analyze the temperature and RH profiles from sounding observations under
399 various AOD levels (Figure 11a-b & d-e). These AOD levels include light pollution
400 ($\text{AOD} < 0.2$), medium pollution ($0.2 < \text{AOD} < 0.5$), and heavy pollution ($\text{AOD} > 0.5$)
401 scenarios. The selection of this threshold is to ensure a balanced sample size for each
402 scenario. All differences in the temperature and RH profiles under different AOD
403 scenarios passed the significance test with $p \leq 0.1$ by the t -test. For the temperature
404 profiles, a higher AOD corresponds to a lower temperature in the upper atmosphere,
405 and vice versa (Figure 11a). However, for the low-level atmosphere, the temperature
406 might first increase as AOD increases and then decrease with AOD as increases. This
407 is associated with aerosol type and optical properties (Che et al., 2024; Mahowald et
408 al., 2011). For the RH vertical profiles, RH increases as AOD increases at all pressure
409 levels (Figure 11b). This may be attributed to aerosol hygroscopic growth effect,
410 leading to a higher AOD (Quan et al., 2018). Notably, since the collocation between
411 MWR and Level 2 sun photometer AOD products from the AERONET is already
412 clear-sky data, the vertical profiles of RH is relatively low. BTs at 22.23 GHz
413 calculated by these vertical profiles from MonoRTM also demonstrate that BTs tend
414 to increase with AOD (Figure 11c). BTs at other frequencies in the K band also show
415 similar trend (not shown here). Similarly, the WRF-Chem output also demonstrates
416 the sensitiveness of temperature and RH vertical profiles to aerosol loading,
417 contributing to statistically significant BT difference under different pollution levels
418 (Figure 11d-f). The above observational evidence indicates that MWR estimate AOD
419 by detecting the temperature and humidity profile differences caused by the presence
420 of aerosols, further verifying the theoretical basis of our technique.

421 Furthermore, our simulation results, illustrated in Figure 12 and 13, indicate that for
422 all frequencies in the K band, BT increases as AOD levels increase. This phenomenon
423 exists in both the daytime and nighttime. Specifically, at 22.23 GHz, BT levels for
424 clean conditions range from 60 K to 80 K, while for polluted conditions they range
425 from 80 to 130 K, showing a statistically significant difference at both daytime and



426 nighttime (Figure 12a & 13a). BT levels at other frequencies support this trend,
427 indicating that BT tends to increase with AOD (Figure 12b-d & 13b-d). The increase
428 of K band BT with AOD might be related to coherent changes of water vapor and
429 aerosols, either due to aerosol absorption of water or meteorological conditions that
430 affect both water vapor and aerosols. In contrast to the observations in the K band, an
431 analysis of the V band frequencies reveals a consistent decrease in BT with the
432 reduction of AOD levels, applicable to both diurnal and nocturnal periods (Figure
433 12e-h & 13e-h), which well corresponds to the cooling effect of aerosols. Notably, at
434 a frequency of 51.76 GHz, the BT levels exhibit a range of 264 K to 270 K under
435 pristine atmospheric conditions, whereas under polluted conditions, these levels are
436 observed to be between 262 K and 265 K. Although the magnitude of this change is
437 less pronounced than that observed in the K band, it still passes the statistical
438 significance ($p \leq 0.1$ by the t -test), indicating a reliable and measurable effect. The
439 above-mentioned conclusion was further verified by simulations lasting from 0000
440 UTC on 3 December 2016 to 0000 UTC on 5 December 2016 (a 48-hour period) with
441 the same settings (not shown).

442 To deepen our understanding of the impact of aerosol loading on longwave radiation,
443 we conducted a comparative analysis using WRF-Chem. By comparing scenarios with
444 aerosol loadings (EXP_AER) and without aerosol loadings (EXP_NOAER), we
445 examined the differences in AOD, surface temperature (ST) and ground downward
446 longwave radiation (GDLR). The findings reveal that higher aerosol concentration
447 levels have a negative effect on ST (Figure 14b & e), particularly during the daytime
448 (Figure 14b), while positively influencing GDLR (Figure 14c & f), especially at
449 nighttime (Figure 14f), which is consistent with the above MonoRTM calculations.



450 **4. Conclusions and Discussions**

451 This study introduces a new method for estimating clear sky AOD using BT
452 measurements in the K and V band obtained from the MWR. By establishing a strong
453 correlation between the photometer AOD and multiple BTs derived from the MWR at
454 the Beijing Nanjiao Meteorological Observatory using a machine learning algorithm,
455 we were able to accurately retrieve nighttime AOD and vertical temperature profiles.
456 This model also well captures the spectral characteristics of AOD with higher
457 Angstrom index for fine-mode dominated AOD and lower Angstrom index for
458 coarse-mode dominated AOD. After applying this model with satisfactory
459 performance, we show that the AOD diurnal cycle and find that AOD values follow a
460 bi-modal diurnal cycle temporal distribution, with a greater peak ~21:00 and a
461 secondary peak at ~03:00, suggesting higher nighttime AOD compared with daytime.
462 The difference between daytime and nighttime AOD observed in the MWR data well
463 agrees with sun and lunar photometer observation as well as particle matter
464 concentration observations.

465 The theoretical basis of our algorithm is also confirmed by analyzing observational
466 vertical profiles of temperature and RH under various AOD levels and WRF-Chem as
467 well as MonoRTM simulations. Observation indicated that the vertical profiles of
468 temperature and RH have statistically significant differences ($p \leq 0.1$) under different
469 AOD levels, suggesting that MWR might estimate AOD by detecting the temperature
470 and humidity profile differences caused by various aerosol loadings. Simulation
471 further indicated a consistent and mostly linear increase in BTs in the K band and
472 decrease in BTs in the V band with AOD (550 nm) across all time periods. Aerosols
473 tend to induce a cooling effect at surface while increasing ground downward
474 longwave radiation, especially at the nighttime.

475 This study holds significant promise for environmental and climate research as MWR
476 BT measurements can be obtained day and night without being hindered by bright



477 surfaces. The methodology developed here can potentially be applied to MWRs in
478 other locations worldwide to retrieve both daytime and nighttime AOD values.
479 However, it is important to note that this investigation is preliminary and may contain
480 uncertainties. It is also applicable under clear sky since during cloudy sky, the
481 downward microwave radiation will be dominated by that emitted by clouds.

482 Moving forward, we aim to explore additional aerosol characteristics that may be
483 inferred from BT measurements, such as aerosol absorption and layer height. This
484 will enhance our understanding of aerosol distribution and properties, ultimately
485 improving our ability to monitor and predict aerosol impacts on climate and the
486 environment.

487



488 **Code and data availability**

489 The sun photometer AOD data was obtained from https://aeronet.gsfc.nasa.gov/new_web/webtool_aod_v3.html, last access: 20 Apr 2024; the lunar photometer
490 AOD data was obtained from https://aeronet.gsfc.nasa.gov/new_web/webtool_aod_v3_lunar.html, last access: 20 Apr 2024; the temperature profile from the ER
491 A-5 reanalysis data was downloaded from <https://cds.climate.copernicus.eu/cdsapp#!/dataset/reanalysis-era5-pressure-levels?tab=overview>, last access: 24 Apr 2024;
492 the MonoRTM source code is available on <https://github.com/AER-RC/monoRTM>, last access 18 Apr 2024. The sounding data obtained from Beijing Meteor
493 ological Station (station ID: 54511) was obtained from <https://weather.uwyo.edu/upperair/bufrfraob.shtml>.

499 **Author contributions**

500 GL and JL conceived the study and wrote the original draft. GL, SY, LZ, and CZ ran
501 the simulation and conducted the corresponding analysis. All authors revised and
502 reviewed the draft.

503 **Competing interests**

504 The authors declare that they have no known competing financial interests or personal
505 relationships that could have appeared to influence the work reported in this paper.

506 **Acknowledgments**

507 The authors thank Pawan Gupta and Elena Lind for their effort in establishing and
508 maintaining Beijing-CAMS AERONET site.

509 **Financial support**



510 This study is funded by the National Natural Science Foundation of China (NSFC) No.
511 42425503 and No. 42175144, and National Key Research and Development Program
512 of China (grant no. 2023YFF0805401).

513

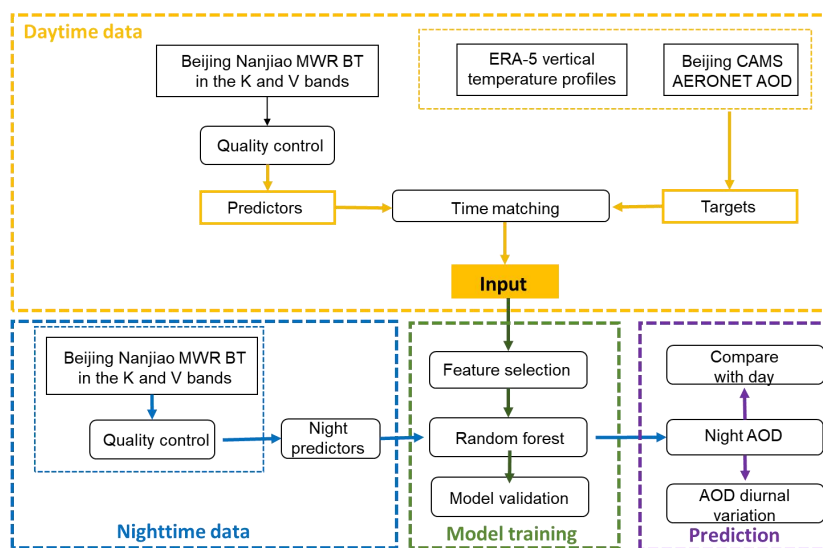
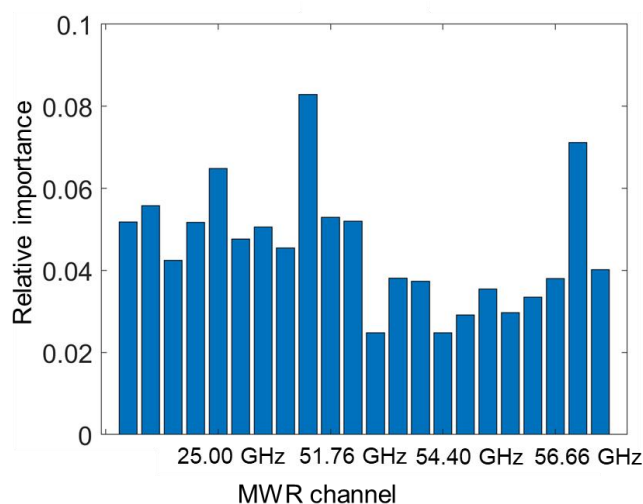


Figure 1. The flowchart for clear sky nighttime AOD retrieval algorithm.



517

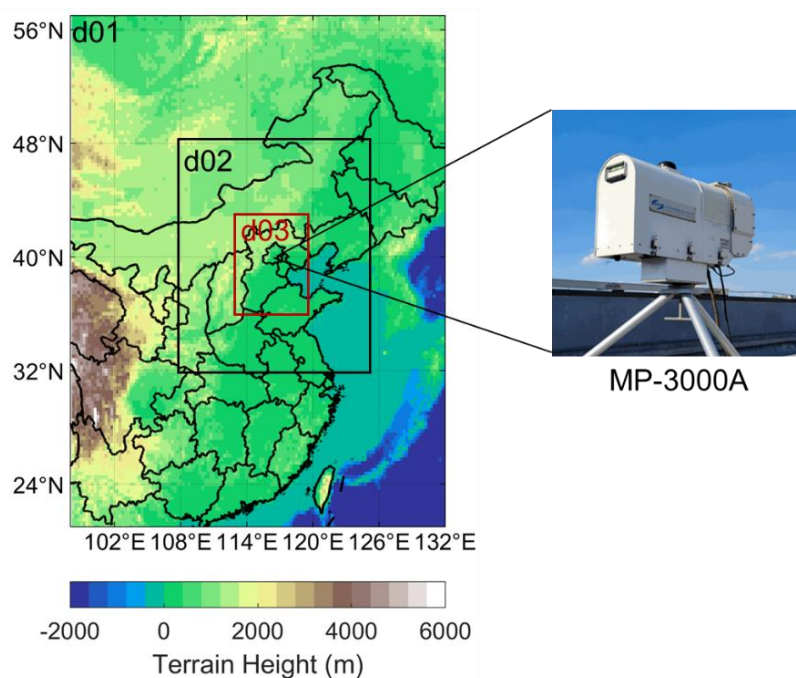
518 **Figure 2.** Relative importance of all BTs in different frequencies measured by MWR
519 in the RFR model. The vertical axis represents relative importance (unitless), and the
520 horizontal axis corresponds to different variable inputs (BTs in different frequencies
521 measured by MWR in the RFR model). These channels include K band (22.23 GHz,
522 22.50 GHz, 23.03 GHz, 23.83 GHz, 25.00 GHz, 26.23 GHz, 28.00 GHz, 30.00 GHz)
523 and V band (51.25 GHz, 51.76 GHz, 52.28 GHz, 52.80 GHz, 53.34 GHz, 53.85 GHz,
524 54.40 GHz, 54.94 GHz, 55.50 GHz, 56.02 GHz, 56.66 GHz, 57.29 GHz, 57.96 GHz,
525 58.80 GHz).

526

527



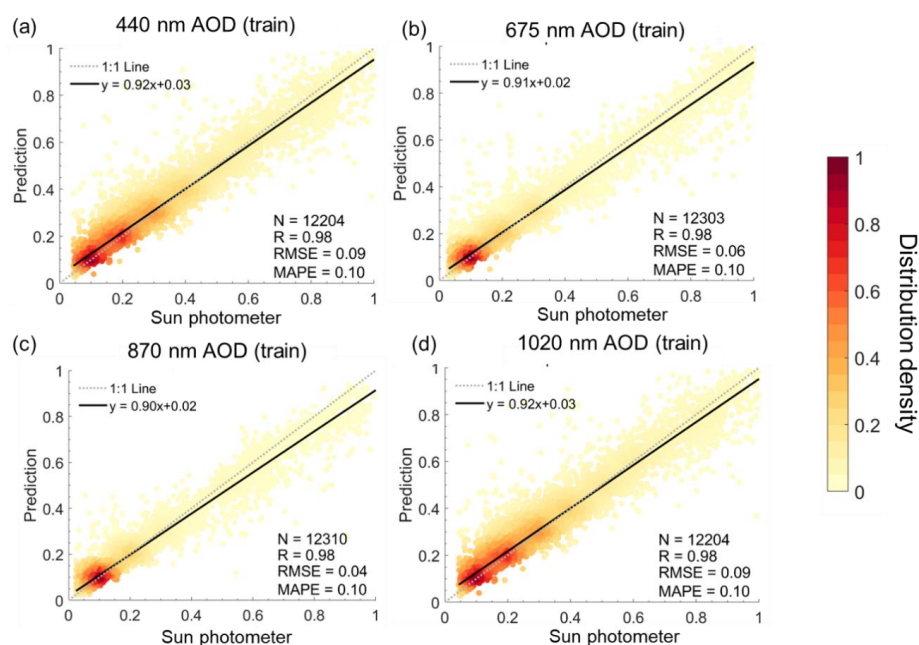
528



529

530 **Figure 3.** Simulation domains (left panel) of the WRF-Chem experiments. The MWR
 531 (right panel) used in this study is located in domain 3. This domain has a spatial
 532 resolution of 10 km. The MP-3000A MWR by Radiometrics is deployed at the
 533 Beijing Nanjiao Meteorological Observatory (39.80°N, 116.47°E) in China for
 534 brightness temperature (BT) measurements.

535

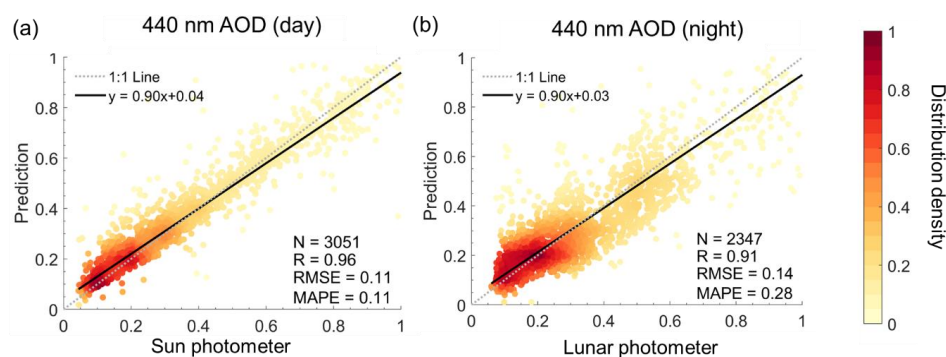


536

537 **Figure 4.** Density scatterplots of daytime AOD in the train set of MWR and sun
 538 photometer with (a) 440 nm, (b) 675 nm, (c) 870 nm, and (d) 1020 nm. The dashed
 539 dark gray line represents the 1:1 line, and the black solid line represents the linear
 540 regression line.

541

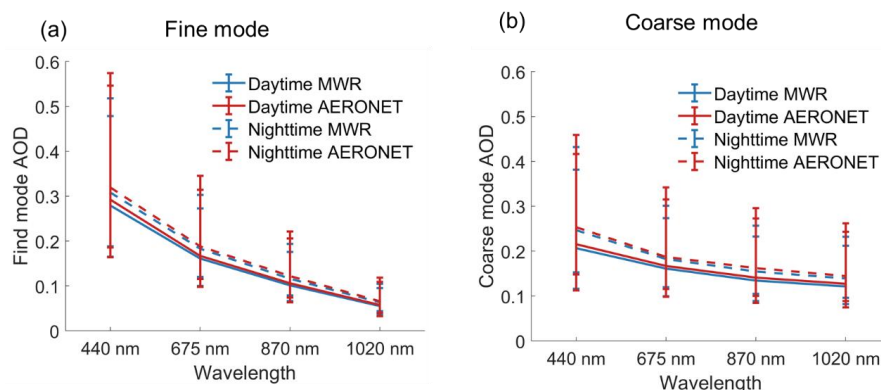
542



543

544 **Figure 5.** Density scatterplots of 440 nm AOD in the test set of MWR and the
 545 photometer with (a) daytime, and (b) nighttime. The dashed dark gray line represents
 546 the 1:1 line, and the black solid line represents the linear regression line. Note that the
 547 daytime corresponds to 6:00 am to 6:00 pm for the local time (UTC+8), and nighttime
 548 corresponds to the remaining time.

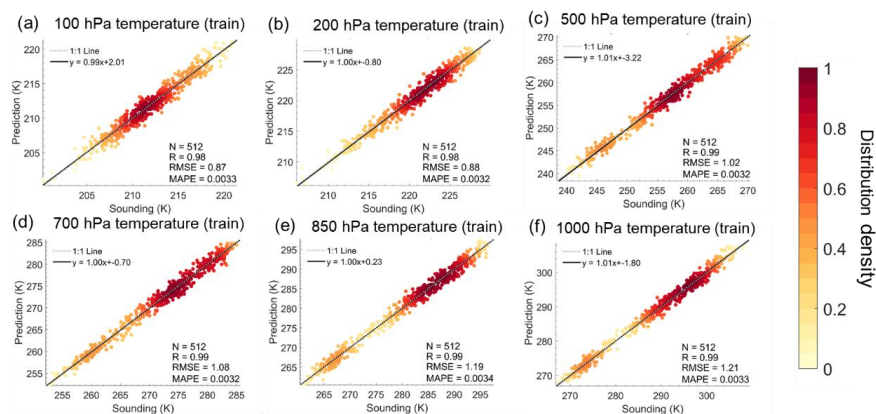
549



550

551 **Figure 6.** The relationship between wavelength and its corresponding AOD for
 552 MWR-based (blue lines) and the photometer (red lines) in the daytime (solid lines)
 553 and nighttime (dashed lines) for the (a) fine mode particles (440 nm to 870 nm
 554 Angstrom index > 1), and (b) coarse mode particles (440 nm to 870 nm Angstrom
 555 index < 1). The upper bound of the error bar is the 25th percentile, the middle is the
 556 median, and the lower bound is the 75th percentile.

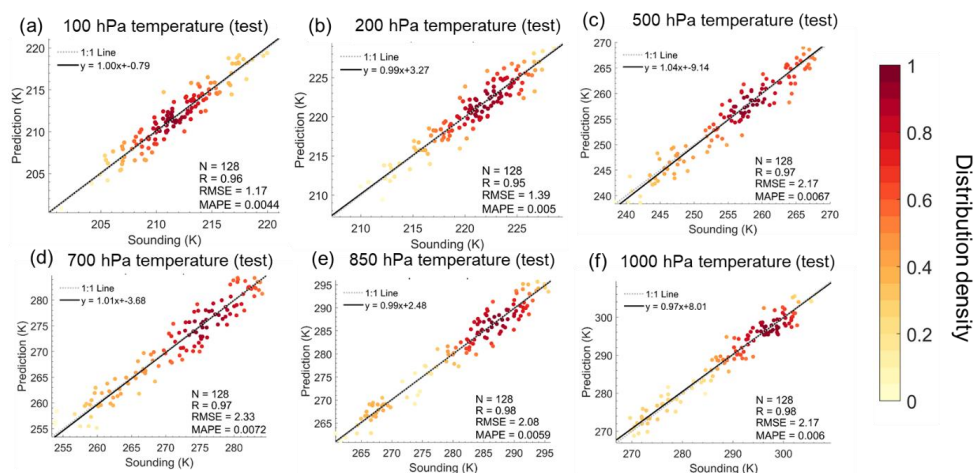
557



558

559 **Figure 7.** Density scatterplots of the vertical temperature profile in the train set of
 560 MWR and sounding data at (a) 100 hPa, (b) 200 hPa, (c) 500 hPa, (d) 700 hPa, (e)
 561 850 hPa, and (f) 1000 hPa. The dashed dark gray line represents the 1:1 line, and the
 562 black solid line represents the linear regression line.

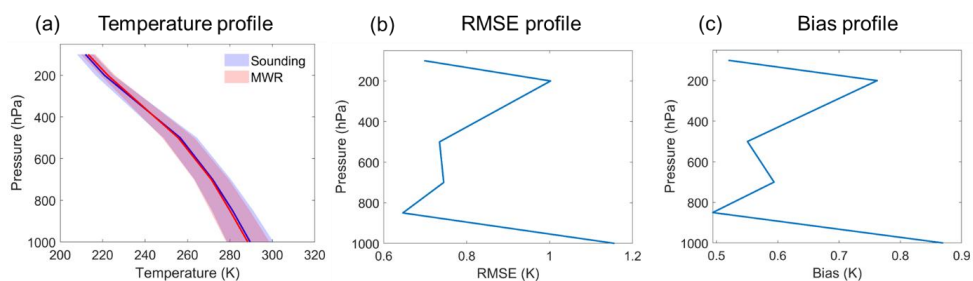
563



564

565 **Figure 8.** Density scatterplots of the vertical temperature profile in the test set of
 566 MWR and sounding data at (a) 100 hPa, (b) 200 hPa, (c) 500 hPa, (d) 700 hPa, (e)
 567 850 hPa, and (f) 1000 hPa. The dashed dark gray line represents the 1:1 line, and the
 568 black solid line represents the linear regression line.

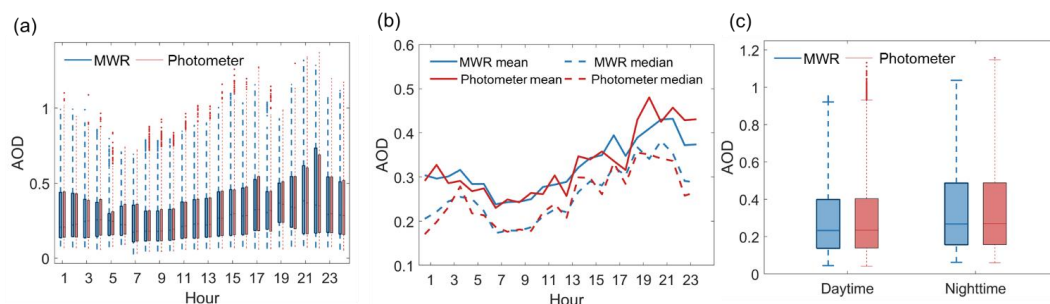
569



570

571 **Figure 9.** (a) Climatological mean vertical temperature profiles from sounding (the
 572 blue shading and line) and MWR (the red shading and line). (b) RMSE vertical profile
 573 calculated between sounding and MWR temperature, and (c) Similar to (b), but for the
 574 bias vertical profile.

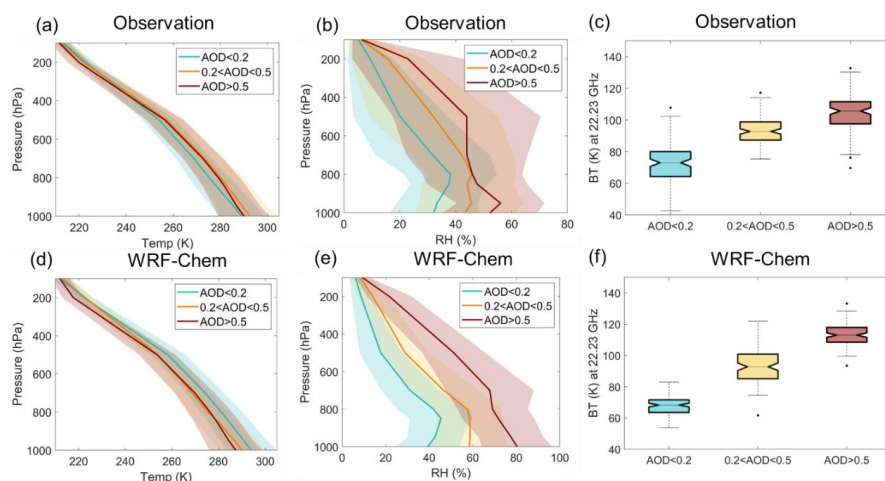
575



576

577 **Figure 10.** The diurnal cycle of MWR AOD and photometer AOD at 440nm. (a) The
578 boxplot of hourly MWR AOD (red boxplots) and photometer AOD (blue boxplots).
579 The small dots represent outliers greater than $q_{75} + 1.5(q_{75} - q_{25})$ or less than
580 $q_{25} - 1.5(q_{75} - q_{25})$, where q_{75} and q_{25} correspond to 75th and 25th percentile. (b)
581 The time series of mean AOD (solid lines) and median AOD (dashed lines) of MWR
582 AOD (red lines) and photometer AOD (blue lines). (c) The boxplot of daytime and
583 nighttime AOD. Blue boxes correspond to MWR data, and red boxes correspond to
584 photometer data.

585

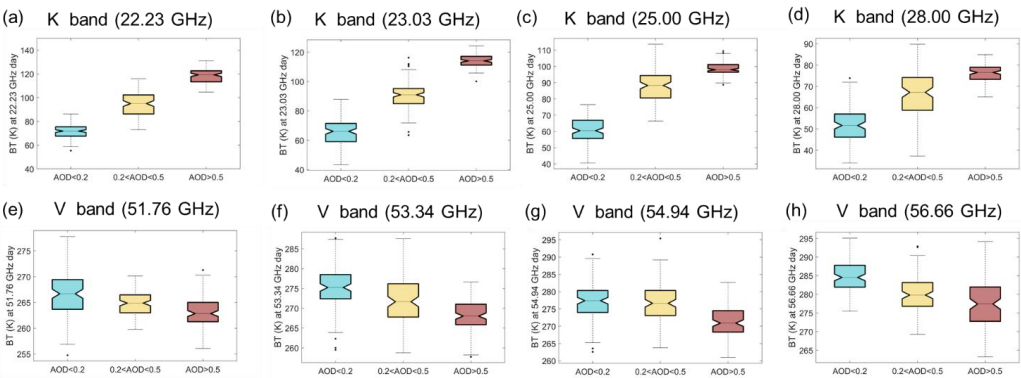


586

587 **Figure 11.** (a-b) The observational vertical profiles of temperature (Temp, unit: K)
 588 and relative humidity (RH, unit: %) under various AOD levels. The cyan, orange, and
 589 red solid lines correspond to low-level polluted scenarios (AOD<0.2), mid-level
 590 polluted scenarios (0.2<AOD<0.5), and high-level polluted scenarios (AOD>0.5). (c)
 591 Their corresponding brightness temperature (BT, unit: K) at 22.23 GHz calculated by
 592 MonoRTM. (d-f) Similar to a-c, but for the WRF-Chem simulation. The shadings
 593 represent the spread of samples with one standard deviation. All differences have
 594 passed the significance test of $p\text{-value} \leq 0.01$ by Student's t -test.

595

596



597

598 **Figure 12.** The boxplots of relationship between BT and AOD at 550 nm when fixing
599 the surface temperature at 270-275 K from 0000 UTC 18 December 2016 to 0000
600 UTC 20 December 2016 in the WRF-Chem simulation. The frequencies of BT are (a)
601 22.23 GHz, (b) 23.03 GHz, (c) 25.00 GHz, (d) 28.00 GHz, (e) 51.76 GHz, (f) 53.34
602 GHz, (g) 54.94 GHz, and (h) 56.66 GHz during the daytime.

603

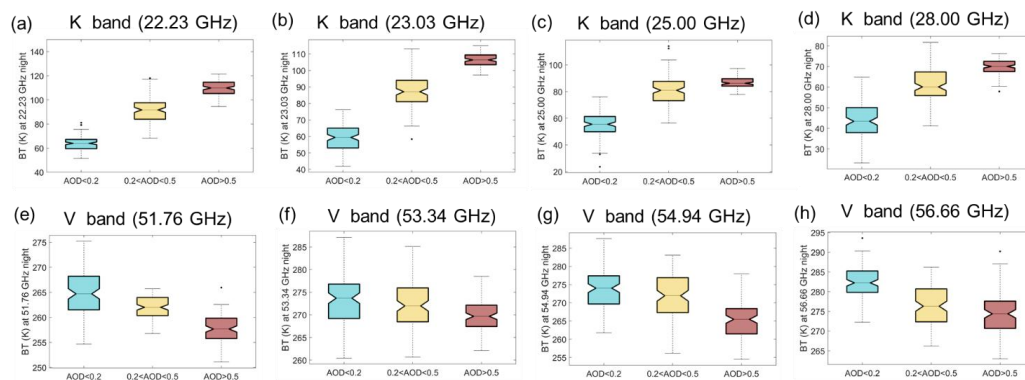
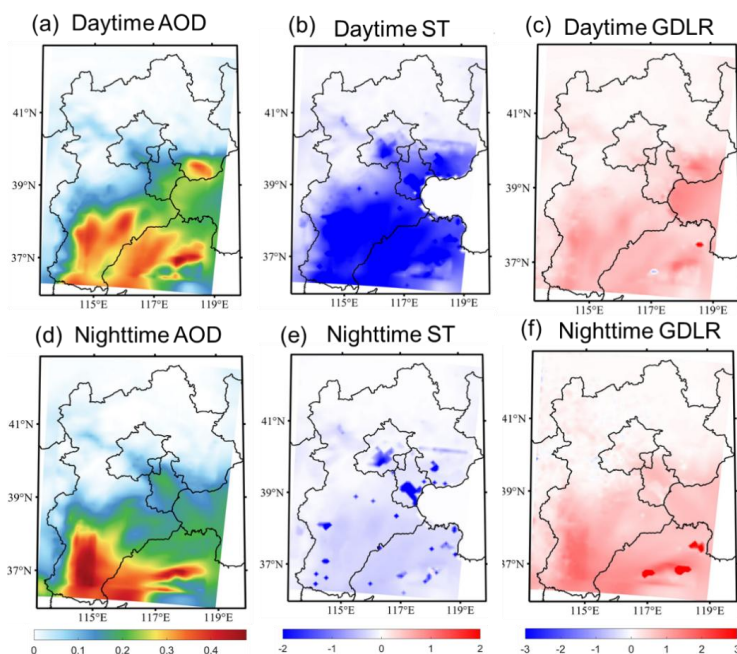


Figure 13. Similar to Figure 12, but for the nighttime.



608

609 **Figure 14.** The difference of (a, d) aerosol optical depth (AOD), (b, e) surface
610 temperature (ST), and (c, f) ground downward longwave radiation (GDLR) between
611 EXP_AER and EXP_NOAER experiments (EXP_AER-EXP_NOAER) during the
612 (a-c) daytime and (d-f) nighttime. The daytime corresponds to the period from 2200
613 UTC 18 December 2016 to 1000 UTC 19 December 2016. The nighttime corresponds
614 to the period from 1000 UTC 19 December 2016 to 2200 UTC 19 December 2016.

615



616 References

- 617 Adebisi, A., Kok, J. F., Murray, B. J., Ryder, C. L., Stuut, J. B. W., Kahn, R. A., Knippertz, P.,
618 Formenti, P., Mahowald, N. M., Garcia-Pando, C. P., Klose, M., Ansmann, A., Samset, B. H., Ito, A.,
619 Balkanski, Y., Di Biagio, C., Romanias, M. N., Huang, Y., and Meng, J.: A review of coarse mineral
620 dust in the Earth system, *AEOLIAN RESEARCH*, 60, 10.1016/j.aeolia.2022.100849, 2023.
621 Arola, A., Eck, T. F., Huttunen, J., Lehtinen, K. E. J., Lindfors, A. V., Myhre, G., Smirnov, A., Tripathi,
622 S. N., and Yu, H.: Influence of observed diurnal cycles of aerosol optical depth on aerosol direct
623 radiative effect, *ATMOSPHERIC CHEMISTRY AND PHYSICS*, 13, 7895-7901,
624 10.5194/acp-13-7895-2013, 2013.
625 Balmes, K. A., Fu, Q., and Thorsen, T. J.: The Diurnal Variation of the Aerosol Optical Depth at the
626 ARM SGP Site, *EARTH AND SPACE SCIENCE*, 8, 10.1029/2021EA001852, 2021.
627 Barreto, A., Roman, R., Cuevas, E., Berjon, A. J., Fernando Almansa, A., Toledano, C., Gonzalez, R.,
628 Hernandez, Y., Blarel, L., Goloub, P., Guirado, C., and Yela, M.: Assessment of nocturnal aerosol
629 optical depth from lunar photometry at the Izana high mountain observatory, *ATMOSPHERIC*
630 *MEASUREMENT TECHNIQUES*, 10, 3007-3019, 10.5194/amt-10-3007-2017, 2017.
631 Barreto, A., Cuevas, E., Granados-Munoz, M.-J., Alados-Arboledas, L., Romero, P. M., Groebner, J.,
632 Kouremeti, N., Almansa, A. F., Stone, T., Toledano, C., Roman, R., Sorokin, M., Holben, B., Canini,
633 M., and Yela, M.: The new sun-sky-lunar Cimel CE318-T multiband photometer - a comprehensive
634 performance evaluation, *ATMOSPHERIC MEASUREMENT TECHNIQUES*, 9, 631-654,
635 10.5194/amt-9-631-2016, 2016.
636 Berkoff, T. A., Sorokin, M., Stone, T., Eck, T. F., Hoff, R., Welton, E., and Holben, B.: Nocturnal
637 Aerosol Optical Depth Measurements with a Small-Aperture Automated Photometer Using the Moon
638 as a Light Source, *JAtOT*, 28, 1297-1306, 10.1175/JTECH-D-10-05036.1, 2011.
639 Bianco, L., Cimini, D., Marzano, F. S., and Ware, R.: Combining microwave radiometer and wind
640 profiler radar measurements for high-resolution atmospheric humidity profiling, *JAtOT*, 22, 949-965,
641 10.1175/JTECH1771.1, 2005.
642 Brock, C. A., Wagner, N. L., Anderson, B. E., Beyersdorf, A., Campuzano-Jost, P., Day, D. A., Diskin,
643 G. S., Gordon, T. D., Jimenez, J. L., Lack, D. A., Liao, J., Markovic, M. Z., Middlebrook, A. M.,
644 Perring, A. E., Richardson, M. S., Schwarz, J. P., Welti, A., Ziemba, L. D., and Murphy, D. M.:
645 Aerosol optical properties in the southeastern United States in summer - Part 2: Sensitivity of aerosol
646 optical depth to relative humidity and aerosol parameters, *ATMOSPHERIC CHEMISTRY AND*
647 *PHYSICS*, 16, 5009-5019, 10.5194/acp-16-5009-2016, 2016.
648 Cachorro, V. E., Romero, P. M., Toledano, C., Cuevas, E., and de Frutos, A. M.: The fictitious diurnal
649 cycle of aerosol optical depth: A new approach for "in situ" calibration and correction of AOD data
650 series, *GEOPHYSICAL RESEARCH LETTERS*, 31, 10.1029/2004GL019651, 2004.
651 Cachorro, V. E., Toledano, C., Berjón, A., de Frutos, A. M., Torres, B., Sorribas, M., and Laulainen, N.
652 S.: An "in situ" calibration correction procedure (KCICLO) based on AOD diurnal cycle:: Application
653 to AERONET -: El Arenosillo (Spain) AOD data series, *JOURNAL OF GEOPHYSICAL*
654 *RESEARCH-ATMOSPHERES*, 113, 10.1029/2007JD009673, 2008.
655 Chaikovsky, A. P., Bril, A. I., Fedarenka, A. S., Peshcharankou, V. A., Denisov, S. V., Dick, V. P.,
656 Asipenka, F. P., Miatselskaya, N. S., Balin, Y. S., Kokhanenko, G. P., Penner, I. E., Samoilova, S. V.,
657 Klemasheva, M. G., Nasonov, S. V., Zhamsueva, G. S., Zayakhanov, A. S., Tsydygov, V. V., Batbold,



- 658 A., Azzaya, D., Enkhbat, E., Oyunchimeg, D., Anh, N. X., Thanh, P. X., Hiep, N. V., Tuan, A. D., and
659 Chen, B.: Synergy of Ground-Based and Satellite Optical Remote Measurements for Studying
660 Atmospheric Aerosols, *JApSp*, 86, 1092-1099, 10.1007/s10812-020-00945-z, 2020.
661 Che, H. Z., Xia, X. G., Zhao, H. J., Li, L., Gui, K., Zheng, Y., Song, J. J., Qi, B., Zhu, J., Miao, Y. C.,
662 Wang, Y. Q., Wang, Z. L., Wang, H., Dubovik, O., Holben, B., Chen, H. B., Shi, G. Y., and Zhang, X.
663 Y.: Aerosol optical and radiative properties and their environmental effects in China: A review,
664 *EARTH-SCIENCE REVIEWS*, 248, 10.1016/j.earscirev.2023.104634, 2024.
665 Chen, A. N. and Zhao, C. F.: Progress of aerosol direct radiative forcing, *CHINESE SCIENCE*
666 *BULLETIN-CHINESE*, 69, 30-44, 10.1360/TB-2023-0375, 2024.
667 Chen, Y., Chen, S. Y., Zhou, J., Zhao, D., Bi, H. R., Zhang, Y., Alam, K., Yu, H. P., Yang, Y. X., and
668 Chen, J. Y.: A super dust storm enhanced by radiative feedback, *NPJ CLIMATE AND*
669 *ATMOSPHERIC SCIENCE*, 6, 10.1038/s41612-023-00418-y, 2023.
670 Cimini, D., Hewison, T. J., Martin, L., Güldner, J., Gaffard, C., and Marzano, F. S.: Temperature and
671 humidity profile retrievals from ground-based microwave radiometers during TUC, *MetZe*, 15, 45-56,
672 10.1127/0941-2948/2006/0099, 2006.
673 Clarisse, L., Clerbaux, C., Franco, B., Hadji-Lazaro, J., Whitburn, S., Kopp, A. K., Hurtmans, D., and
674 Coheur, P. F.: A Decadal Data Set of Global Atmospheric Dust Retrieved From IASI Satellite
675 Measurements, *JOURNAL OF GEOPHYSICAL RESEARCH-ATMOSPHERES*, 124, 1618-1647,
676 10.1029/2018JD029701, 2019.
677 Clough, S. A., Shephard, M. W., Mlawer, E., Delamere, J. S., Iacono, M., Cady-Pereira, K., Boukabara,
678 S., and Brown, P. D.: Atmospheric radiative transfer modeling: a summary of the AER codes, *J. Quant.*
679 *Spectros. Radiat. Transfer*, 91, 233-244, 10.1016/j.jqsrt.2004.05.058, 2005.
680 Colarco, P. R., Nowottnick, E. P., Randles, C. A., Yi, B. Q., Yang, P., Kim, K. M., Smith, J. A., and
681 Bardeen, C. G.: Impact of radiatively interactive dust aerosols in the NASA GEOS-5 climate model:
682 Sensitivity to dust particle shape and refractive index, *JOURNAL OF GEOPHYSICAL*
683 *RESEARCH-ATMOSPHERES*, 119, 753-786, 10.1002/2013JD020046, 2014.
684 Crippa, M., Guizzardi, D., Muntean, M., Schaaf, E., Dentener, F., van Aardenne, J. A., Monni, S.,
685 Doering, U., Olivier, J. G. J., Pagliari, V., and Janssens-Maenhout, G.: Gridded emissions of air
686 pollutants for the period 1970-2012 within EDGAR v4.3.2, *EARTH SYSTEM SCIENCE DATA*, 10,
687 1987-2013, 10.5194/essd-10-1987-2018, 2018.
688 DeSouza-Machado, S. G., Strow, L. L., Imbiriba, B., McCann, K., Hoff, R. M., Hannon, S. E., Martins,
689 J. V., Tanré, D., Deuzé, J. L., Ducos, F., and Torres, O.: Infrared retrievals of dust using AIRS:
690 Comparisons of optical depths and heights derived for a North African dust storm to other collocated
691 EOS A-Train and surface observations, *JOURNAL OF GEOPHYSICAL*
692 *RESEARCH-ATMOSPHERES*, 115, 10.1029/2009JD012842, 2010.
693 Dufresne, J. L., Gautier, C., Ricchiazzi, P., and Fouquart, Y.: Longwave scattering effects of mineral
694 aerosols, *JOURNAL OF THE ATMOSPHERIC SCIENCES*, 59, 1959-1966,
695 10.1175/1520-0469(2002)059<1959:LSEOMA>2.0.CO;2, 2002.
696 Ebr, J., Karpov, S., Eliášek, J., Blazek, J., Cuniffe, R., Ebrová, I., Janecek, P., Jelínek, M., Jurysek, J.,
697 Mandát, D., Masek, M., Pech, M., Prouza, M., and Trávníček, P.: A New Method for Aerosol
698 Measurement Using Wide-field Photometry, *ASTRONOMICAL JOURNAL*, 162,
699 10.3847/1538-3881/abf7b1, 2021.



- 700 Fan, J. W., Wang, Y., Rosenfeld, D., and Liu, X. H.: Review of Aerosol-Cloud Interactions:
701 Mechanisms, Significance, and Challenges, *JOURNAL OF THE ATMOSPHERIC SCIENCES*, 73,
702 4221-4252, 10.1175/JAS-D-16-0037.1, 2016.
- 703 Feng, Y., Wang, H., Rasch, P. J., Zhang, K., Lin, W., Tang, Q., Xie, S., Hamilton, D. S., Mahowald, N.,
704 and Yu, H.: Global Dust Cycle and Direct Radiative Effect in E3SM Version 1: Impact of Increasing
705 Model Resolution, *JOURNAL OF ADVANCES IN MODELING EARTH SYSTEMS*, 14,
706 10.1029/2021MS002909, 2022.
- 707 Ge, J., Huang, J., Weng, F., and Sun, W.: Effects of dust storms on microwave radiation based on
708 satellite observation and model simulation over the Taklamakan desert, *ATMOSPHERIC*
709 *CHEMISTRY AND PHYSICS*, 8, 4903-4909, 10.5194/acp-8-4903-2008, 2008.
- 710 Ghan, S., Wang, M. H., Zhang, S. P., Ferrachat, S., Gettelman, A., Griesfeller, J., Kipling, Z., Lohmann,
711 U., Morrison, H., Neubauer, D., Partridge, D. G., Stier, P., Takemura, T., Wang, H. L., and Zhang, K.:
712 Challenges in constraining anthropogenic aerosol effects on cloud radiative forcing using present-day
713 spatiotemporal variability, *PROCEEDINGS OF THE NATIONAL ACADEMY OF SCIENCES OF*
714 *THE UNITED STATES OF AMERICA*, 113, 5804-5811, 10.1073/pnas.1514036113, 2016.
- 715 Greenwald, T. J., Bennartz, R., Lebsock, M., and Teixeira, J.: An Uncertainty Data Set for Passive
716 Microwave Satellite Observations of Warm Cloud Liquid Water Path, *JOURNAL OF GEOPHYSICAL*
717 *RESEARCH-ATMOSPHERES*, 123, 3668-3687, 10.1002/2017JD027638, 2018.
- 718 Guo, J. P., Xia, F., Zhang, Y., Liu, H., Li, J., Lou, M. Y., He, J., Yan, Y., Wang, F., Min, M., and Zhai,
719 P. M.: Impact of diurnal variability and meteorological factors on the $PM_{2.5}$ - AOD
720 relationship: Implications for $PM_{2.5}$ remote sensing, *ENVIRONMENTAL POLLUTION*,
721 221, 94-104, 10.1016/j.envpol.2016.11.043, 2017.
- 722 Hong, G., Yang, P., Weng, F. Z., and Liu, Q. H.: Microwave scattering properties of sand particles:
723 Application to the simulation of microwave radiances over sandstorms, *J. Quant. Spectros. Radiat.*
724 *Transfer*, 109, 684-702, 10.1016/j.jqsrt.2007.08.018, 2008.
- 725 Huang, J. P., Ge, J. M., and Weng, F. Z.: Detection of Asia dust storms using multisensor satellite
726 measurements, *REMOTE SENSING OF ENVIRONMENT*, 110, 186-191, 10.1016/j.rse.2007.02.022,
727 2007.
- 728 Huang, J. P., Wang, T. H., Wang, W. C., Li, Z. Q., and Yan, H. R.: Climate effects of dust aerosols
729 over East Asian arid and semiarid regions, *JOURNAL OF GEOPHYSICAL*
730 *RESEARCH-ATMOSPHERES*, 119, 11398-11416, 10.1002/2014JD021796, 2014.
- 731 Ivanescu, L. and O'Neill, N. T.: Multi-star calibration in starphotometry, *ATMOSPHERIC*
732 *MEASUREMENT TECHNIQUES*, 16, 6111-6121, 10.5194/amt-16-6111-2023, 2023.
- 733 Ivanescu, L., Baibakov, K., O'Neill, N. T., Blanchet, J. P., and Schulz, K. H.: Accuracy in
734 starphotometry, *ATMOSPHERIC MEASUREMENT TECHNIQUES*, 14, 6561-6599,
735 10.5194/amt-14-6561-2021, 2021.
- 736 Jiang, M., Chen, L., He, Y., Hu, X., Liu, M., and Zhang, P.: Nighttime aerosol optical depth retrievals
737 from VIIRS day/night band data, *National Remote Sensing Bulletin*, 26, 493-504, 2022.
- 738 Jiang, X., Wang, Y., Wang, L., Tao, M., Wang, J., Zhou, M., Bai, X., and Gui, L.: Characteristics of
739 Daytime-And-Nighttime AOD Differences Over China: A Perspective From CALIOP Satellite
740 Observations and GEOS-Chem Model Simulations, *JOURNAL OF GEOPHYSICAL*
741 *RESEARCH-ATMOSPHERES*, 129, 10.1029/2023JD039158, 2024.



742 Klüser, L., Kleiber, P., Holzer-Popp, T., and Grassian, V. H.: Desert dust observation from space -
743 Application of measured mineral component infrared extinction spectra, *ATMOSPHERIC*
744 *ENVIRONMENT*, 54, 419-427, 10.1016/j.atmosenv.2012.02.011, 2012.
745 Knupp, K. R., Ware, R., Cimini, D., Vandenberghe, F., Vivekanandan, J., Westwater, E., Coleman, T.,
746 and Phillips, D.: Ground-Based Passive Microwave Profiling during Dynamic Weather Conditions,
747 *JATOT*, 26, 1057-1073, 10.1175/2008JTECHA1150.1, 2009.
748 Kremser, S., Thomason, L. W., von Hobe, M., Hermann, M., Deshler, T., Timmreck, C., Toohey, M.,
749 Stenke, A., Schwarz, J. P., Weigel, R., Fueglistaler, S., Prata, F. J., Vernier, J. P., Schlager, H., Barnes,
750 J. E., Antuña-Marrero, J. C., Fairlie, D., Palm, M., Mahieu, E., Notholt, J., Rex, M., Bingen, C.,
751 Vanhellemont, F., Bourassa, A., Plane, J. M. C., Klocke, D., Carn, S. A., Clarisse, L., Trickl, T., Neely,
752 R., James, A. D., Rieger, L., Wilson, J. C., and Meland, B.: Stratospheric aerosol-Observations,
753 processes, and impact on climate, *REVIEWS OF GEOPHYSICS*, 54, 278-335,
754 10.1002/2015RG000511, 2016.
755 Levy, R. C., Mattoo, S., Munchak, L. A., Remer, L. A., Sayer, A. M., Patadia, F., and Hsu, N. C.: The
756 Collection 6 MODIS aerosol products over land and ocean, *ATMOSPHERIC MEASUREMENT*
757 *TECHNIQUES*, 6, 2989-3034, 10.5194/amt-6-2989-2013, 2013.
758 Li, J., Li, C. C., Zhao, C. S., and Su, T. N.: Changes in surface aerosol extinction trends over China
759 during 1980-2013 inferred from quality-controlled visibility data, *GEOPHYSICAL RESEARCH*
760 *LETTERS*, 43, 8713-8719, 10.1002/2016GL070201, 2016a.
761 Li, J., Carlson, B. E., Yung, Y. L., Lv, D. R., Hansen, J., Penner, J. E., Liao, H., Ramaswamy, V., Kahn,
762 R. A., Zhang, P., Dubovik, O., Ding, A. J., Lacis, A. A., Zhang, L., and Dong, Y. M.: Scattering and
763 absorbing aerosols in the climate system, *NATURE REVIEWS EARTH & ENVIRONMENT*, 3,
764 363-379, 10.1038/s43017-022-00296-7, 2022.
765 Li, M., Zhang, Q., Kurokawa, J., Woo, J. H., He, K. B., Lu, Z. F., Ohara, T., Song, Y., Streets, D. G.,
766 Carmichael, G. R., Cheng, Y. F., Hong, C. P., Huo, H., Jiang, X. J., Kang, S. C., Liu, F., Su, H., and
767 Zheng, B.: MIX: a mosaic Asian anthropogenic emission inventory under the international
768 collaboration framework of the MICS-Asia and HTAP, *ATMOSPHERIC CHEMISTRY AND*
769 *PHYSICS*, 17, 935-963, 10.5194/acp-17-935-2017, 2017.
770 Li, W. J., Shao, L. Y., Zhang, D. Z., Ro, C. U., Hu, M., Bi, X. H., Geng, H., Matsuki, A., Niu, H. Y.,
771 and Chen, J. M.: A review of single aerosol particle studies in the atmosphere of East Asia:
772 morphology, mixing state, source, and heterogeneous reactions, *JOURNAL OF CLEANER*
773 *PRODUCTION*, 112, 1330-1349, 10.1016/j.jclepro.2015.04.050, 2016b.
774 Li, Z. Q., Wang, Y., Guo, J. P., Zhao, C. F., Cribb, M., Dong, X. Q., Fan, J. W., Gong, D. Y., Huang, J.
775 P., Jiang, M. J., Jiang, Y. Q., Lee, S. S., Li, H., Li, J. M., Liu, J. J., Qian, Y., Rosenfeld, D., Shan, S. Y.,
776 Sun, Y. L., Wang, H. J., Xin, J. Y., Yan, X., Yang, X., Yang, X. Q., Zhang, F., and Zheng, Y. T.: East
777 Asian Study of Tropospheric Aerosols and their Impact on Regional Clouds, Precipitation, and Climate
778 (EAST-AIR_{CPC}), *JOURNAL OF GEOPHYSICAL RESEARCH-ATMOSPHERES*, 124,
779 13026-13054, 10.1029/2019JD030758, 2019.
780 Liu, C. S., Shen, X. X., and Gao, W.: Intercomparison of CALIOP, MODIS, and AERONET aerosol
781 optical depth over China during the past decade, *IJRS*, 39, 7251-7275,
782 10.1080/01431161.2018.1466070, 2018.
783 Liu, G. Y., Li, J., Li, J., Yue, S., and Zhou, R. L.: Estimation of Nighttime Aerosol Optical Depths
784 Using Atmospheric Infrared Sounder Longwave Radiances, *GEOPHYSICAL RESEARCH LETTERS*,
785 51, 10.1029/2023GL108120, 2024.



- 786 Mahowald, N., Ward, D. S., Kloster, S., Flanner, M. G., Heald, C. L., Heavens, N. G., Hess, P. G.,
787 Lamarque, J. F., and Chuang, P. Y.: Aerosol Impacts on Climate and Biogeochemistry, in: ANNUAL
788 REVIEW OF ENVIRONMENT AND RESOURCES, VOL 36, edited by: Gadgil, A., and Liverman, D.
789 M., 45-74, 10.1146/annurev-environ-042009-094507, 2011.
- 790 Matsui, H., Hamilton, D. S., and Mahowald, N. M.: Black carbon radiative effects highly sensitive to
791 emitted particle size when resolving mixing-state diversity, NATURE COMMUNICATIONS, 9,
792 10.1038/s41467-018-05635-1, 2018.
- 793 Meng, Y., Zhou, J., Wang, Z., Tang, W., Ma, J., Zhang, T., and Long, Z.: Retrieval of nighttime
794 aerosol optical depth by simultaneous consideration of artificial and natural light sources, SCIENCE
795 OF THE TOTAL ENVIRONMENT, 896, 10.1016/j.scitotenv.2023.166354, 2023.
- 796 Mhawish, A., Banerjee, T., Broday, D. M., Misra, A., and Tripathi, S. N.: Evaluation of MODIS
797 Collection 6 aerosol retrieval algorithms over Indo-Gangetic Plain: Implications of aerosols types and
798 mass loading, REMOTE SENSING OF ENVIRONMENT, 201, 297-313, 10.1016/j.rse.2017.09.016,
799 2017.
- 800 Mitra, A. K., Sharma, A. K., Soni, V. K., and Kundu, P. K.: Characteristics of recent dust storms over
801 the Indian region using real time multi-satellite observations from the direct broadcast receiving system
802 at IMD, AdSpR, 51, 1195-1203, 10.1016/j.asr.2012.11.017, 2013.
- 803 Nembrini, S., König, I. R., and Wright, M. N.: The revival of the Gini importance?,
804 BIOINFORMATICS, 34, 3711-3718, 10.1093/bioinformatics/bty373, 2018.
- 805 Omar, A. H., Winker, D. M., Tackett, J. L., Giles, D. M., Kar, J., Liu, Z., Vaughan, M. A., Powell, K.
806 A., and Trepte, C. R.: CALIOP and AERONET aerosol optical depth comparisons: One size fits none,
807 JOURNAL OF GEOPHYSICAL RESEARCH-ATMOSPHERES, 118, 4748-4766, 10.1002/jgrd.50330,
808 2013.
- 809 Panicker, A. S., Pandithurai, G., Safai, P. D., and Kewat, S.: Observations of enhanced aerosol
810 longwave radiative forcing over an urban environment, GEOPHYSICAL RESEARCH LETTERS, 35,
811 10.1029/2007GL032879, 2008.
- 812 Payne, V. H., Mlawer, E. J., Cady-Pereira, K. E., and Moncet, J. L.: Water Vapor Continuum
813 Absorption in the Microwave, IEEE TRANSACTIONS ON GEOSCIENCE AND REMOTE
814 SENSING, 49, 2194-2208, 10.1109/TGRS.2010.2091416, 2011.
- 815 Pérez-Ramírez, D., Lyamani, H., Olmo, F. J., and Alados-Arboledas, L.: Improvements in star
816 photometry for aerosol characterizations, JAER, 42, 737-745, 10.1016/j.jaerosci.2011.06.010, 2011.
- 817 Pérez-Ramírez, D., Lyamani, H., Olmo, F. J., Whiteman, D. N., and Alados-Arboledas, L.: Columnar
818 aerosol properties from sun-and-star photometry: statistical comparisons and day-to-night dynamic,
819 ATMOSPHERIC CHEMISTRY AND PHYSICS, 12, 9719-9738, 10.5194/acp-12-9719-2012, 2012.
- 820 Pérez-Ramírez, D., Ruiz, B., Aceituno, J., Olmo, F. J., and Alados-Arboledas, L.: Application of
821 Sun/star photometry to derive the aerosol optical depth, IJRS, 29, 5113-5132,
822 10.1080/01431160802036425, 2008.
- 823 Pérez-Ramírez, D., Lyamani, H., Smirnov, A., O'Neill, N. T., Veselovskii, I., Whiteman, D. N., Olmo,
824 F. J., and Alados-Arboledas, L.: Statistical study of day and night hourly patterns of columnar aerosol
825 properties using sun and star photometry, REMOTE SENSING OF CLOUDS AND THE
826 ATMOSPHERE XXI, WOS:000391488200014, 10.1117/12.2242372, 2016.
- 827 Pérez-Ramírez, D., Veselovskii, I., Whiteman, D. N., Suvorina, A., Korenskiy, M., Kolgotin, A.,
828 Holben, B., Dubovik, O., Siniuk, A., and Alados-Arboledas, L.: High temporal resolution estimates of
829 columnar aerosol microphysical parameters from spectrum of aerosol optical depth by linear estimation:



830 application to long-term AERONET and star-photometry measurements, *ATMOSPHERIC*
831 *MEASUREMENT TECHNIQUES*, 8, 3117-3133, 10.5194/amt-8-3117-2015, 2015.
832 Perrone, M. R., Lorusso, A., and Romano, S.: Diurnal and nocturnal aerosol properties by AERONET
833 sun-sky-lunar photometer measurements along four years, *ATMOSPHERIC RESEARCH*, 265,
834 10.1016/j.atmosres.2021.105889, 2022.
835 Pierangelo, C., Mishchenko, M., Balkanski, Y., and Chédin, A.: Retrieving the effective radius of
836 Saharan dust coarse mode from AIRS -: art. no. L20813, *GEOPHYSICAL RESEARCH LETTERS*, 32,
837 10.1029/2005GL023425, 2005.
838 Pierangelo, C., Chédin, A., Heilliette, S., Jacquinet-Husson, N., and Armante, R.: Dust altitude and
839 infrared optical depth from AIRS, *ATMOSPHERIC CHEMISTRY AND PHYSICS*, 4, 1813-1822,
840 10.5194/acp-4-1813-2004, 2004.
841 Quan, J. N., Jiang, C. L., Xin, J. Y., Zhao, X. J., Jia, X. C., Liu, Q., Gao, Y., and Chen, D.: Evaluation
842 of satellite aerosol retrievals with in situ aircraft and ground measurements: Contribution of relative
843 humidity, *ATMOSPHERIC RESEARCH*, 212, 1-5, 10.1016/j.atmosres.2018.04.024, 2018.
844 Riemer, N., Ault, A. P., West, M., Craig, R. L., and Curtis, J. H.: Aerosol Mixing State: Measurements,
845 Modeling, and Impacts, *REVIEWS OF GEOPHYSICS*, 57, 187-249, 10.1029/2018RG000615, 2019.
846 Rogers, R. R., Vaughan, M. A., Hostetler, C. A., Burton, S. P., Ferrare, R. A., Young, S. A., Hair, J. W.,
847 Obland, M. D., Harper, D. B., Cook, A. L., and Winker, D. M.: Looking through the haze: evaluating
848 the CALIPSO level 2 aerosol optical depth using airborne high spectral resolution lidar data,
849 *ATMOSPHERIC MEASUREMENT TECHNIQUES*, 7, 4317-4340, 10.5194/amt-7-4317-2014, 2014.
850 Santa Maria, M. and Winker, D.: Sampling uncertainties in observing the global aerosol with a
851 nadir-viewing satellite lidar, *LIDAR REMOTE SENSING FOR INDUSTRY AND*
852 *ENVIRONMENTAL MONITORING V*, WOS:000227658800037, 10.1117/12.583098, 2005.
853 Sayer, A. M., Hsu, N. C., Lee, J., Kim, W. V., and Dutcher, S. T.: Validation, Stability, and
854 Consistency of MODIS Collection 6.1 and VIIRS Version 1 Deep Blue Aerosol Data Over Land,
855 *JOURNAL OF GEOPHYSICAL RESEARCH-ATMOSPHERES*, 124, 4658-4688,
856 10.1029/2018JD029598, 2019.
857 Seinfeld, J. H., Bretherton, C., Carslaw, K. S., Coe, H., DeMott, P. J., Dunlea, E. J., Feingold, G., Ghan,
858 S., Guenther, A. B., Kahn, R., Kraucunas, I., Kreidenweis, S. M., Molina, M. J., Nenes, A., Penner, J.
859 E., Prather, K. A., Ramanathan, V., Ramaswamy, V., Rasch, P. J., Ravishankara, A. R., Rosenfeld, D.,
860 Stephens, G., and Wood, R.: Improving our fundamental understanding of the role of aerosol-cloud
861 interactions in the climate system, *PROCEEDINGS OF THE NATIONAL ACADEMY OF*
862 *SCIENCES OF THE UNITED STATES OF AMERICA*, 113, 5781-5790, 10.1073/pnas.1514043113,
863 2016.
864 Sinyuk, A., Holben, B. N., Eck, T. F., Giles, D. M., Slutsker, I., Korkin, S., Schafer, J. S., Smirnov, A.,
865 Sorokin, M., and Lyapustin, A.: The AERONET Version 3 aerosol retrieval algorithm, associated
866 uncertainties and comparisons to Version 2, *ATMOSPHERIC MEASUREMENT TECHNIQUES*, 13,
867 3375-3411, 10.5194/amt-13-3375-2020, 2020.
868 Song, Q. Q., Zhang, Z. B., Yu, H. B., Kok, J. F., Di Biagio, C., Albani, S., Zheng, J. Y., and Ding, J. C.:
869 Size-resolved dust direct radiative effect efficiency derived from satellite observations,
870 *ATMOSPHERIC CHEMISTRY AND PHYSICS*, 22, 13115-13135, 10.5194/acp-22-13115-2022,
871 2022.
872 Stenchikov, G., Robock, A., Ramaswamy, V., Schwarzkopf, M. D., Hamilton, K., and Ramachandran,
873 S.: Arctic Oscillation response to the 1991 Mount Pinatubo eruption: Effects of volcanic aerosols and



874 ozone depletion, JOURNAL OF GEOPHYSICAL RESEARCH-ATMOSPHERES, 107,
875 10.1029/2002JD002090, 2002.

876 Su, X., Huang, Y. H., Wang, L. C., Cao, M. D., and Feng, L.: Validation and diurnal variation
877 evaluation of MERRA-2 multiple aerosol properties on a global scale, ATMOSPHERIC
878 ENVIRONMENT, 311, 10.1016/j.atmosenv.2023.120019, 2023.

879 Sun, J. Y. T., Veeffkind, P., van Velthoven, P., and Levelt, P. F.: Aerosol Absorption Over Land
880 Derived From the Ultra-Violet Aerosol Index by Deep Learning, IEEE JOURNAL OF SELECTED
881 TOPICS IN APPLIED EARTH OBSERVATIONS AND REMOTE SENSING, 14, 9692-9710,
882 10.1109/JSTARS.2021.3108669, 2021.

883 Svetnik, V., Liaw, A., Tong, C., Culberson, J. C., Sheridan, R. P., and Feuston, B. P.: Random forest: A
884 classification and regression tool for compound classification and QSAR modeling, J Chem Inf
885 Comput Sci, 43, 1947-1958, 10.1021/ci034160g, 2003.

886 Tindan, J. Z., Jin, Q. J., and Pu, B.: Understanding day-night differences in dust aerosols over the dust
887 belt of North Africa, the Middle East, and Asia, ATMOSPHERIC CHEMISTRY AND PHYSICS, 23,
888 5435-5466, 10.5194/acp-23-5435-2023, 2023.

889 Varga, A. J. and Breuer, H.: Evaluation of convective parameters derived from pressure level and
890 native ERA5 data and different resolution WRF climate simulations over Central Europe, CLIMATE
891 DYNAMICS, 58, 1569-1585, 10.1007/s00382-021-05979-3, 2022.

892 Visioni, D., Bednarz, E. M., Lee, W. R., Kravitz, B., Jones, A., Haywood, J. M., and MacMartin, D. G.:
893 Climate response to off-equatorial stratospheric sulfur injections in three Earth system models - Part 1:
894 Experimental protocols and surface changes, ATMOSPHERIC CHEMISTRY AND PHYSICS, 23,
895 663-685, 10.5194/acp-23-663-2023, 2023.

896 Wang, H. Z., Zhang, R., Wang, G. H., An, Y. Z., and Jin, B. G.: Quality control of Argo temperature
897 and salinity observation profiles, CHINESE JOURNAL OF GEOPHYSICS-CHINESE EDITION, 55,
898 577-588, 10.6038/j.issn.0001-5733.2012.02.020, 2012.

899 Wang, J., Xia, X. G., Wang, P. C., and Christopher, S. A.: Diurnal variability of dust aerosol optical
900 thickness and Angstrom exponent over dust source regions in China, GEOPHYSICAL RESEARCH
901 LETTERS, 31, 10.1029/2004GL019580, 2004.

902 Wang, L. T., Wei, Z., Yang, J., Zhang, Y., Zhang, F. F., Su, J., Meng, C. C., and Zhang, Q.: The 2013
903 severe haze over southern Hebei, China: model evaluation, source apportionment, and policy
904 implications, ATMOSPHERIC CHEMISTRY AND PHYSICS, 14, 3151-3173,
905 10.5194/acp-14-3151-2014, 2014.

906 Wang, N., Hu, Y., Li, X. M., Kang, C., and Yan, L.: AOD Derivation from SDGSAT-1/GLI Dataset in
907 Mega-City Area, REMOTE SENSING, 15, 10.3390/rs15051343, 2023.

908 Wang, X., Mu, X., and Yan, G.: Quantitative Analysis of Aerosol Influence on Suomi-NPP VIIRS
909 Nighttime Light in China, IEEE JOURNAL OF SELECTED TOPICS IN APPLIED EARTH
910 OBSERVATIONS AND REMOTE SENSING, 13, 3557-3568, 10.1109/JSTARS.2020.3003480, 2020.

911 Wei, L. Y., Wang, Y., Liu, S., Zhang, G., and Wang, B.: Distinct roles of land cover in regulating
912 spatial variabilities of temperature responses to radiative effects of aerosols and clouds,
913 ENVIRONMENTAL RESEARCH LETTERS, 16, 10.1088/1748-9326/ac3f04, 2021.

914 Yang, Z. M., Zdanski, C., Farkas, D., Bang, J., and Williams, H.: Evaluation of Aerosol Optical Depth
915 (AOD) and PM_{2.5} associations for air quality assessment, REMOTE SENSING
916 APPLICATIONS-SOCIETY AND ENVIRONMENT, 20, 10.1016/j.rsase.2020.100396, 2020.



- 917 Yu, Y., Kalashnikova, O. V., Garay, M. J., Lee, H., Choi, M., Okin, G. S., Yorks, J. E., Campbell, J. R.,
918 and Marquis, J.: A global analysis of diurnal variability in dust and dust mixture using CATS
919 observations, *ATMOSPHERIC CHEMISTRY AND PHYSICS*, 21, 1427-1447,
920 10.5194/acp-21-1427-2021, 2021.
- 921 Zhang, J., Jaker, S. L., Reid, J. S., Miller, S. D., Solbrig, J., and Toth, T. D.: Characterization and
922 application of artificial light sources for nighttime aerosol optical depth retrievals using the Visible
923 Infrared Imager Radiometer Suite Day/Night Band, *ATMOSPHERIC MEASUREMENT*
924 *TECHNIQUES*, 12, 3209-3222, 10.5194/amt-12-3209-2019, 2019.
- 925 Zhang, L., Liu, M., He, W., Xia, X., Yu, H., Li, S., and Li, J.: Ground Passive Microwave Remote
926 Sensing of Atmospheric Profiles Using WRF Simulations and Machine Learning Techniques, *Journal*
927 *of Meteorological Research*, 38, 680-692, 10.1007/s13351-024-4004-2, 2024.
- 928 Zhang, L. L., Liu, M. J., He, W. Y., Xia, X. A., Yu, H. N., Li, S. X., Li, J.: Ground Passive
929 Microwave Remote Sensing of Atmospheric Profiles Using WRF Simulations and Machine Learning
930 Techniques, *Journal of Meteorological Research*, 10.1007/s13351-024-4004-2, 2024.
- 931 Zhang, X. Y., Xu, X. Y., Chen, H. S., Hu, X. M., and Gao, L.: Dust-planetary boundary layer
932 interactions amplified by entrainment and advections, *ATMOSPHERIC RESEARCH*, 278,
933 10.1016/j.atmosres.2022.106359, 2022.
- 934 Zheng, J. Y., Zhang, Z. B., Garnier, A., Yu, H. B., Song, Q. Q., Wang, C. X., Dubuisson, P., and Di
935 Biagio, C.: The thermal infrared optical depth of mineral dust retrieved from integrated CALIOP and
936 IIR observations, *REMOTE SENSING OF ENVIRONMENT*, 270, 10.1016/j.rse.2021.112841, 2022.
- 937 Zheng, J. Y., Zhang, Z. B., Yu, H. B., Garnier, A., Song, Q. Q., Wang, C. X., Di Biagio, C., Kok, J. F.,
938 Derimian, Y., and Ryder, C.: Thermal infrared dust optical depth and coarse-mode effective diameter
939 over oceans retrieved from collocated MODIS and CALIOP observations, *ATMOSPHERIC*
940 *CHEMISTRY AND PHYSICS*, 23, 8271-8304, 10.5194/acp-23-8271-2023, 2023.
- 941 Zhou, M., Wang, J., Chen, X., Xu, X., Colarco, P. R., Miller, S. D., Reid, J. S., Kondragunta, S., Giles,
942 D. M., and Holben, B.: Nighttime smoke aerosol optical depth over US rural areas: First retrieval from
943 VIIRS moonlight observations, *REMOTE SENSING OF ENVIRONMENT*, 267,
944 10.1016/j.rse.2021.112717, 2021.

945